Internal gravity wave radiation into weakly stratified fluid

B. R. Sutherland[a)]
Department of Applied Mathematics and Theoretical Physics, University of Cambridge, Silver Street, CB3 9EW, Cambridge, England

(Received 9 August 1995; accepted 23 October 1995)

It is shown by way of nonlinear numerical simulations of flow restricted to two dimensions that a compact wavepacket of large-amplitude internal gravity waves incident upon a weakly stratified region in which the buoyancy frequency is less than the frequency of the wavepacket may partially transmit energy into this region through the generation of a wavepacket of lower frequency. In part, the transmission of waves occurs due to the transient nature of the forcing by the incident wavepacket, but if the amplitude of the wavepacket is moderately large, weakly nonlinear effects may act to significantly increase the proportion of the wavepacket that is transmitted. For a range of simulations initialized with wavepackets of different amplitude and vertical extent, the characteristics of the reflected and transmitted waves are analyzed and reflection coefficients are calculated. An explanation for how the nonlinear transmission mechanism operates is given by demonstrating that the wave induced mean-flow, which is shown to be approximately equal to the horizontal wave pseudomomentum expressed in Eulerian variables, acts to adjust the frequency of the incident waves. © *1996 American Institute of Physics.* [S1070-6631(96)02002-2]

I. INTRODUCTION

Under many geophysical circumstances, internal gravity waves (IGW) may be confined to a duct (or waveguide) within which the medium is strongly stratified and outside of which the stratification is weak. For example, ducted IGW have been observed to be confined below regions of low static stability in the upper troposphere,[1] and IGW confined to the thermocline region in the ocean have been observed to propagate long horizontal distances away from their source.[2] The characteristics of ducted IGW in a horizontally homogeneous medium have been examined in linear theory, where typically it is supposed that the waves are manifest as normal modes (e.g., for a general discussion see Gill,[3] Sec. 6.10). Weakly nonlinear theories have extended the normal mode approach for shallow water,[4,5] deep water,[4,6] and water of finite depth,[7,8] and with some success these have reproduced the observed characteristics of the long time evolution of ducted IGW of large horizontal extent in the ocean.[9,10] Exact solutions of the fully nonlinear equations for horizontally bounded, finite-amplitude IGW in a channel of infinite horizontal extent have been found by Long,[11] and these have been applied to examine numerically the nonlinear evolution of topographically generated IGW (for example, Scinocca and Peltier,[12] among others). Generally, most weakly and fully nonlinear theories of ducted IGW assume that the horizontal extent of the waves is large or comparable to the vertical extent of the waveguide, but these approaches do not suitably describe the transient behavior of a compact wavepacket, the vertical extent of which is small compared with the vertical extent of the strongly stratified region.

In linear theory, the temporal behavior of a wavepacket of small-amplitude IGW incident upon a region where the fluid becomes weakly stratified was first studied by Bretherton,[13] who applied the WKB approximation to the equations of motion in a medium where the vertical variations of the squared buoyancy frequency N^2 were small over a wavelength. His analysis also included a treatment of background shear which is not considered in detail here. He showed that a wavepacket incident upon a level z_r where N equals the frequency of the waves is reflected in a finite time. Both the ''critical level'' and the ''evanescent level'' have been used to refer to z_r, but, because the former terminology has also been used to describe the height at which the mean-flow equals the phase speed of an incident wave, the latter terminology is used here. An analytic expression for the path followed by the incident and reflected wavepacket may be determined by ray theory except near an evanescent level, where a caustic forms and the wave amplitude is described locally by an Airy function (for example, see Lighthill,[14] Secs. 4.5, 4.11). In particular, ray theory shows that upward propagating IGW, reflect in such a way that the phase tilt of the waves becomes more vertical as the evanescent level is approached.

WKB based theories rest on the assumption that N decreases gradually compared with the vertical wavelength of IGW, and it is not well understood to what extent the theories remain valid for cases in which N varies rapidly over a vertical wavelength or, indeed, for cases in which the waves are of non-negligible amplitude.

In this paper it is demonstrated in theory and by way of fully nonlinear numerical simulations restricted to two dimensions that a compact IGW wavepacket incident upon an evanescent level may be transmitted across this presumed barrier in the form of a propagating wavepacket of smaller amplitude. For incident waves of small amplitude, the transmission mechanism is attributed to transient forcing and may be understood by linear theory. For incident waves of large amplitude, however, it will be shown that under a robust range of conditions a greater proportion of the initial wavepacket is capable of penetrating the evanescent level by a

[a)]Fax: [44] 1223 337918; phone: [44] 1223 337900; e-mail: brs21@damtp.cam.ac.uk

 1070-6631/96/8(2)/430/12/$6.00

weakly nonlinear mechanism in which the wave induced mean-flow modulates the frequency of the incident waves. In neither case is the transmission of waves into weakly stratified fluid related to the phenomena of tunneling or anomalous frequency dispersion (such as that studied recently by Dostenko,[15] who has examined IGW confined to two pycnoclines in the ocean), because the transmitted waves, once generated, propagate upward indefinitely in uniformly stratified fluid subject only to dispersion, viscous dissipation, and thermal diffusion.

In section II the initial value problem and the details of the model employed to solve the fully nonlinear equations of motion are described. The various diagnostic tools that are used to study the characteristics of the initial IGW wavepacket and of the reflected and transmitted waves are also discussed here. These include consideration of the finite-amplitude expression for the horizontal wave pseudomomentum, an explicit definition for which is provided at the end of this section. In section III results of the nonlinear simulations are presented. In particular, the evolution of small-amplitude IGW incident upon weakly stratified fluid is considered and the fraction of the initial wavepacket that is reflected from this region is compared with that predicted heuristically from linear theory. Simulations of the evolution of large-amplitude IGW incident upon an evanescent level demonstrate how nonlinear effects enhance the transmission of the waves. The results of a range of simulations are analyzed in order to demonstrate how the nonlinear mechanism is affected by changes in the characteristics of the initial wavepacket and of the background density profile. In section IV an explanation of how the nonlinear mechanism operates is provided. Therein it will be shown that the pseudomomentum of moderately large-amplitude IGW in an Eulerian framework is negligibly different from the wave induced mean-flow. The significance of these results applied to geophysical circumstances is remarked upon in section V.

II. DESCRIPTION OF THE PROBLEM AND LINEAR THEORY

Throughout this work an initial value problem is solved in which a horizontally periodic IGW wavepacket of finite vertical extent is superimposed at the outset of each nonlinear simulation on a stationary stratified fluid in which N^2 is constant over the vertical extent of the wavepacket.

In order to unambiguously determine the characteristics of IGW incident to and propagating away from an evanescent level, the background profile of the squared buoyancy frequency N^2 is taken to be constant for small and large z. Specifically, the piecewise linear form of N^2 is given by

$$N^2(z;J,R)=\begin{cases} J_B(=1), & z\leqslant -R, \\ J+(J-J_B)(z)/R & -R<z\leqslant 0, \\ J, & z>0, \end{cases} \tag{1}$$

in which $N^2=J_B$ for small z, $N^2=J$ for large z and N^2 varies linearly between J_B and J over a distance R. An example of an N^2 profile which is defined by parameters $J_B=1$, $J=0.6$ and $R=5$ is shown in Figure 1(a).

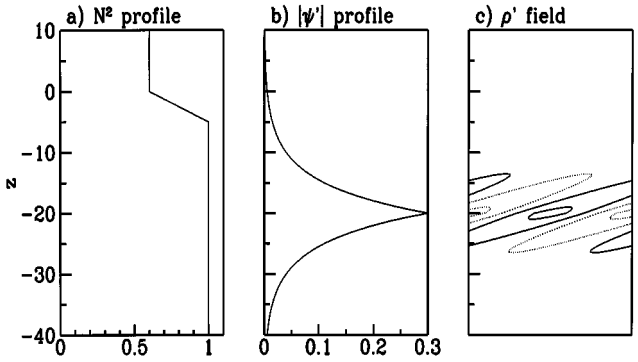

FIG. 1. An example of the initial state of a simulation: (a) $N^2(z)$ profile for the case with $J=0.6$ and $R=5$, (b) the streamfunction amplitude of the initial wavepacket characterized by $A=0.15$ and $D=5$, (c) and the fluctuation density field shown by contours of interval 0.2 corresponding to the initial wavepacket of wavenumber vector $(k_x,k_z)=(1,-0.7071)$. Positive (negative) values are illustrated by solid (dashed) lines.

The wavepacket that is superimposed on the basic state at the start of each simulation is given in terms of the streamfunction by

$$\psi(x,z)=2\ \mathrm{Re}\{A\ \exp(-|z-z_0|/D)\exp[\imath(k_x x+k_z z)]\}, \tag{2}$$

in which k_x and k_z are the horizontal and vertical wavenumbers, respectively, A determines the wavepacket amplitude, and D is the vertical extent of the wavepacket which is centered about $z=z_0\ll -R$. Only upward propagating wavepackets are considered here, and for these k_z is negative. The envelope of the initial wavepacket defined with parameters $A=0.15$, $D=5$, and $z_0=-20$ is shown in Figure 1(b).

The fluctuation density field ρ' is expressed nondimensionally in terms of the vertical displacement of fluid particles from their equilibrium position. For initialization, an approximate expression, valid for $|Dk_z|\gg 1$ and $A\ll 1$, is used to define ρ' in terms of the streamfunction by using the identity for plane IGW of horizontal phase speed c_{px} in uniformly stratified fluid with $N^2=J_B$:

$$\rho'=-(1/c_{px})\psi. \tag{3}$$

Using the dispersion relationship for IGW, ρ' is given explicitly by

$$\rho'(x,z)=-2\ \mathrm{Re}\{A|\vec{k}|/\sqrt{J_B}\ \exp(-|z-z_0|/D) \times\exp[\imath(k_x x+k_z z)]\}, \tag{4}$$

in which $|\vec{k}|$ represents the magnitude of the wavenumber vector. Figure 1(c) shows the fluctuation density field of an IGW wavepacket defined by parameters $A=0.15$, $D=5$, $z_0=-20$, $k_x=1$, and $k_z=-\sqrt{2}/2\simeq -0.7071$. Contours are given by an interval of 0.2.

IGW in which the wavepacket envelope varies vertically as a top hat function or a Gaussian have also be studied, but the exponential envelope given by equation (2) is a useful form for analytic study, and it emulates the far field behavior of unbounded normal modes which decrease exponentially where N^2 and the background horizontal velocity are constant.

The nonlinear simulations are performed by numerically solving the primitive equations for incompressible, Boussinesq flow that is restricted to two spatial dimensions. Any effects of background rotation are ignored. The fully nonlinear equations for momentum conservation are

$$\frac{Du_\star}{Dt_\star} = -\frac{1}{\rho_0}\frac{\partial p'_\star}{\partial x_\star} + \nu\nabla^2 u_\star, \tag{5}$$

$$\frac{Dw_\star}{Dt_\star} = -\frac{1}{\rho_0}\frac{\partial p'_\star}{\partial z_\star} - \frac{g}{\rho_0}\rho'_\star + \nu\nabla^2 w_\star, \tag{6}$$

and the equation expressing the conservation of internal energy is

$$\frac{D\rho'_\star}{Dt_\star} = \frac{N_\star^2}{g} w_\star + \kappa\nabla^2\rho'_\star. \tag{7}$$

Here the ''star'' subscript is used to indicate fields in dimensional form. Here $D/Dt_\star = \partial/\partial t_\star + u_\star\partial/\partial x_\star + w_\star\partial/\partial z_\star$ is the material derivative, $u_\star$ and $w_\star$ are the horizontal and vertical velocities, respectively, $\rho'_\star$ is the fluctuation density, and the fluctuation pressure $p'_\star$ is the total pressure minus the background pressure $\bar{p}_\star(z)$ that is in hydrostatic balance with the background density $\bar{\rho}_\star(z)$. The constant ρ_0 is a characteristic value of $\bar{\rho}_\star$. The squared buoyancy frequency is $N_\star^2 = -(g/\rho_0)d\bar{\rho}_\star/dz_\star$. The physical constants in the equations are the gravitational acceleration g, the kinematic viscosity ν, and the thermal diffusivity κ.

These equations are represented numerically in a model based on the methodology developed by Smyth and Peltier[16] for the study of the evolution of Kelvin-Helmholtz and Holmboe waves. Equations (5), (6), and (7) are re-expressed in nondimensional form by the substitutions $(x_\star, z_\star) \to \mathscr{L}(x,z)$, $t_\star \to (\mathscr{L}/\mathscr{U})t$, $(u_\star, w_\star) \to \mathscr{U}(u,w)$, $\rho'_\star \to (\rho_0\mathscr{L}/\mathscr{H})\rho'$, $\bar{\rho}_\star \to (\rho_0\mathscr{L}/\mathscr{H})\bar{\rho}$, and $p'_\star \to (\rho_0\mathscr{U}^2)p'$, in which $\mathscr{L}$ and $\mathscr{U}$ are characteristic length- and velocity-scales, respectively, and $\mathscr{H}$ is the length-scale of background density variations with height. For the validity of the Boussinesq approximation, $\mathscr{H} \gg \mathscr{L}$. With these substitutions, the nondimensional form of the equations become

$$\frac{Du}{Dt} = -\frac{\partial p'}{\partial x} + \frac{1}{\mathrm{Re}}\nabla^2 u, \tag{8}$$

$$\frac{Dw}{Dt} = -\frac{\partial p'}{\partial z} - J_B\rho' + \frac{1}{\mathrm{Re}}\nabla^2 w, \tag{9}$$

and

$$\frac{D\rho'}{Dt} = N^2 w + \frac{1}{\mathrm{Re\,Pr}}\nabla^2\rho'. \tag{10}$$

Here $\mathrm{Re} = \mathscr{U}\mathscr{L}/\nu$ is the Reynolds number, $\mathrm{Pr} = \nu/\kappa$ is the Prandtl number, and $J_B = (g/\mathscr{H})(\mathscr{L}/\mathscr{U})^2$ is a characteristic value of the nondimensional form of the squared buoyancy frequency. Although defined similarly to the bulk Richardson number, J_B is not a measure of the stability of stratified flow in the presence of background shear because the characteristic scales $\mathscr{L}$ and $\mathscr{U}$ are not determined from the vertical structure of the background horizontal flow $U(z)$ which is taken to be constant. The scales $\mathscr{L}$ and $\mathscr{U}$ are defined so that the initial IGW have horizontal wavenumber $k_x = 1$ and the stratification below $z = -R$ is characterized by $J_B = 1$.

Most of the simulations discussed herein are performed at high Reynolds number with $\mathrm{Re} = 5000$ and with $\mathrm{Pr} = 1$. The Reynolds number is set to be sufficiently large that viscous effects are negligible, but not so large that the numerical stability of the calculation is forfeit. With these settings of Re and Pr, typically only 2 percent of the initial energy of the flow is lost due to dissipation over the duration of each simulation.

Rather than directly integrate equations (8)–(10), these equations are re-expressed in the vorticity-streamfunction form because the model then reduces to evolution equations for only two coupled fields, namely the vorticity ω and the fluctuation density ρ'. Taking the curl of equations (8) and (9) gives the (nondimensional) vorticity equation,

$$\frac{D\omega}{Dt} = J_B\rho'_x + \frac{1}{\mathrm{Re}}\nabla^2\omega, \tag{11}$$

in which $\omega = u_z - w_x$ is the spanwise component of vorticity. The streamfunction is found by inverting the elliptic differential equation,

$$\nabla^2\psi = -\omega, \tag{12}$$

and the components of the velocity vector $\vec{u} = (u,w)$ may be determined from $u = -\partial\psi/\partial z$ and $w = \partial\psi/\partial x$.

The domain is assumed to be a horizontally periodic channel with free slip upper and lower boundary conditions. The channel is sufficiently wide, however, that waves are of negligible amplitude near either boundary throughout each simulation. Only solutions of equations (10) and (11) that are periodic in the horizontal are considered, hence the horizontal structure of the dependent fields may be represented in a Fourier basis, so that

$$f(x,z,t) = \sum_{m=-M}^{M} f_m(z,t)\exp(\imath m k_x x), \tag{13}$$

in which f may represent ω or ρ and M determines the limit of horizontal resolution of each field. The vertical structure of the dependent variables is represented in finite difference form so that ω and ρ are sampled at $P+1$ points $z_0, \ldots, z_P$, at regularly spaced intervals spanning the channel of vertical extent L_z, and vertical derivatives are replaced by their second order finite difference equivalent,

$$\frac{\partial f_m(z_p,t)}{\partial z} \equiv \frac{f_m(z_{(p+1)},t) - f_m(z_{(p-1)},t)}{2\Delta z}, \tag{14}$$

in which $\Delta z = L_z/P$. The resulting set of evolution equations is stepped forward in time using a leap-frog method with an Euler backstep taken at regular time intervals to minimize splitting errors. To ensure that the results of the simulations are not sensitive to the spatial resolution, the results of each simulation are compared with those determined by integrating the equations of motion for fields at twice the vertical resolution. For the simulations presented here, the resolution is found to be adequate for a vertical grid spacing of $\Delta z \simeq 0.15$. The length of the channel is 2π, which is set to support exactly one wavelength of the initial wavepacket.

Simulations have also been performed in which the horizontal extent of the channel is twice as long so that two horizontal wavelengths of the initial wavepacket is supported. In such cases, however, negligible energy was observed to be introduced into superharmonics of wavenumber $\frac{1}{2}$ as the wavepacket evolved.

During each simulation the wavepacket is analyzed with a number of diagnostics that characterize the amplitude, vertical group velocity, and vertical wavenumber of the transmitted and reflected waves. Vertical profiles of the (nondimensional) Reynolds stress $\tau=\overline{u'w'}$ are calculated at regular time intervals in order to demonstrate the direction and intensity of the vertical flux of horizontal momentum by IGW. An estimate of the vertical group velocity c_{gz+} of the transmitted, upward propagating wavepacket is determined by calculating at late times in each simulation the average vertical speed of the centroid of the positive Reynolds stress that is greater than 5% its maximum value. Likewise, an estimate of the vertical group velocity c_{gz-} of the reflected, downward propagating wavepacket is determined by calculating the average vertical speed of the centroid of the negative Reynolds stress that is less than 5% of its minimum value. Specifically, the average speed is found between times $t=95$ and 100. The vertical wavenumber and frequency of the transmitted wavepacket are determined from the phase tilt and horizontal phase speed, respectively, of IGW at the vertical level corresponding to the centroid of the positive Reynolds stress at the end of each simulation (specifically, at time $t=100$).

To study wave, mean-flow interactions and to find suitable values for reflection coefficients of IGW incident upon an evanescent level, it is useful to examine the horizontal pseudomomentum of IGW. The definition of pseudomomentum in linear theory effectively arises from the observation by Bretherton and Garrett[17] (and earlier by Whitham,[18] who developed a Lagrangian formulation for long surface waves) that the energy density $\mathscr{E}$ of IGW is not conserved but varies as the waves move to heights where the speed of the background flow U is different. The nature of the interaction between the waves and the mean-flow is elegantly expressed for small-amplitude IGW in a slowly varying background flow by the conservation of wave action, $A=\mathscr{E}/(\omega-k_xU(z))$, in which $\omega-k_xU$ is the intrinsic frequency of the waves. As the wavepacket moves upward, ω and k_x are constant, but $\omega-k_xU$ varies if $U(z)$ varies with height, z. Because wave action is conserved, the wave energy density $\mathscr{E}$ must change in proportion to the intrinsic frequency. From this principle, conservation laws follow for pseudoenergy $E=A\omega$ (a conserved quantity with the dimensions of energy density) and horizontal pseudomomentum $M=Ak_x$ (a conserved quantity with the dimensions of momentum density). The fluxes $\mathscr{F}_E$ and $\mathscr{F}_M$, respectively, of these quantities must satisfy

$$\frac{\partial}{\partial t}E=-\nabla\cdot\mathscr{F}_E \tag{15}$$

and

$$\frac{\partial}{\partial t}M=-\nabla\cdot\mathscr{F}_M. \tag{16}$$

For small-amplitude waves, it is found that $\mathscr{F}_E=\vec{c_g}E$ and $\mathscr{F}_M=\vec{c_g}M$ in which $\vec{c_g}$ is the group velocity of the IGW. Where the IGW are of large amplitude or the variation of N^2 or U with height is significant over a vertical wavelength, however, the relationships do not necessarily hold and general expressions must be derived for conserved quantities like pseudomomentum and its flux. These may be found in a Lagrangian framework using the generalized Lagrangian mean formulation developed by Andrews and McIntyre.[19,20] The conservation laws may also be expressed in an Eulerian framework through the Hamiltonian techniques developed by McIntyre and Shepherd[21] (see also the review given by Shepherd[22]), although the resulting formulae can have complicated analytic forms that are difficult to compute numerically. The Hamiltonian method has been applied, in particular, to examine two-dimensional Boussinesq and anelastic flow for which conservation laws have been determined by Scinocca and Shepherd.[23] For the purposes of this paper, only the horizontal pseudomomentum M and its vertical flux $\mathscr{F}_z$ in the absence of initial background motion are of interest. Explicitly, M is given in nondimensional form by

$$M=\omega'\left[\mathscr{Z}(\bar{\rho}+\rho')-\mathscr{Z}(\bar{\rho})-\frac{d\mathscr{Z}(\bar{\rho})}{d\bar{\rho}}\rho'\right]+\frac{d\mathscr{Z}(\bar{\rho})}{d\bar{\rho}}\rho'\omega', \tag{17}$$

in which $\mathscr{Z}(\bar{\rho})$ is height as a function of the background density $\bar{\rho}$, and ω' and ρ' are vorticity and density fluctuations, respectively. The horizontally averaged vertical flux of horizontal pseudomomentum is given by

$$\bar{\mathscr{F}}_z=\overline{u'M}+\tau, \tag{18}$$

in which w' is the vertical velocity fluctuation and, as before, τ is the Reynolds stress.

These expressions are useful both as a means of understanding the nonlinear mechanism by which IGW are transmitted across an evanescent level and as a way of quantifying the effectiveness of this mechanism. In general, reflection coefficients $\mathscr{R}$ are calculated at the end of each simulation (at time $t=100$) for a range of simulations with $\mathscr{R}$ defined as the fraction of the total horizontal pseudomomentum associated with waves below $z=0$. Pseudomomentum is chosen as the quantity with which to define $\mathscr{R}$ because, like energy and pseudoenergy, it is accurate to $O(a^2)$ in the incident wave amplitude a, but unlike energy in general, it is conserved following the wave motion even if N^2 varies in space, and it is more accurately calculated numerically than pseudoenergy which involves the computation of differences between large numbers. In practice, it is found that the numerically calculated domain averaged pseudomomentum changes in time, but this change is improved if smaller time steps are taken during the simulations. With the time step employed for the results reported herein, the domain averaged pseudomomentum increases by less than five percent over the duration of each simulation. The value of the reflection coefficient, however, is found to be relatively insensitive to the choice of time step.

TABLE I. Characteristics of the transmitted IGW wavepacket listed for simulations initialized with a range of different parameters A and D defining the amplitude and depth, respectively, of the initial wavepacket, and J and R defining N^2 in terms of its value for $z>0$ and the depth over which the N^2 decreases from $J_B=1$ to J, respectively. In each case the wavenumber of the initial wavepacket is $(k_x,k_z)=(1,-0.7071)$. The vertical group velocity of the reflected, downward propagating wavepacket c_{gz-} and the transmitted, upward propagating wavepacket c_{gz+}, the vertical wavenumber k_{z+}, and the frequency ω_+ of the transmitted wavepacket, and the reflection coefficient $\mathscr{R}$ are determined at the end of each simulation, as described in the text. For comparison, the last row of the table lists the corresponding characteristics for plane IGW in fluid with $N^2=1$ everywhere.

A	D	R	J	c_{gz-}	c_{gz+}	k_{z+}	ω_+	$\mathscr{R}$
0.01	5		1.0		0.38	−0.72	0.81	0.01
0.01	5	0	0.6	−0.37	0.23	−0.38	0.72	0.86
0.15	5		1.0		0.32	−0.60	0.89	0.004
0.15	5	0	0.6	−0.28	0.26	−0.61	0.68	0.78
0.15	8		1.0		0.29	−0.49	0.91	0.002
0.15	8	0	0.6	−0.26	0.24	−0.57	0.70	0.70
0.15	5	10	0.6	−0.30	0.24	−0.65	0.66	0.80
Plane waves					0.385	−0.707	0.817	0

In summary, the group velocity of the upward (c_{gz+}) and downward (c_{gz-}) propagating wavepacket, the vertical wavenumber (k_+) and frequency (ω_+) of the upward propagating wavepacket, and the reflection coefficient ($\mathscr{R}$) are found for a range of simulations the initial states of which are determined by equations (1) and (2) with parameters $A,D,R,$and J (note, however, that when $J=1$ the fluid is uniformly stratified over the whole domain and the value of R is redundant). The wave characteristics are listed for particular simulations in Table I, and in section III entries in the table will be referred to in the course of discussing the results of these cases.

III. RESULTS OF THE NONLINEAR SIMULATIONS

For every simulation discussed here, the amplitude A and vertical extent D of the initial wavepacket vary and the centre of the wavepacket is fixed at $z_0=-20$. Likewise, the vertical wavenumber is fixed with $k_z=-\sqrt{2}/2\simeq-0.7071$, this value being set because, with horizontal wavenumber $k_x=1$, plane IGW of these attributes have the largest upward group velocity, $c_{gz}=2/3\sqrt{3}\simeq0.3849$. The frequency of such plane waves is $\omega=\sqrt{2/3}\simeq0.8165$ and this is referred to hereafter as the frequency of the initial wavepacket. Simulations have been performed for wavepackets of different vertical wavenumber with similar qualitative results, but $k_z=-\sqrt{2}/2$ is examined in detail because, with this value, a small-amplitude wavepacket undergoes the least dispersion.

Before proceeding to discuss the evolution of IGW incident upon an evanescent level a control simulation is performed in which $N^2=1$ everywhere and the initial small-amplitude wavepacket is characterized by $A=0.01$ and $D=5$. Figure 2 illustrates the state to which the wavepacket has evolved by time $t=100$. The profile of the streamfunction amplitude shown in Figure 2(a) shows that the peak amplitude of the wavepacket has decreased moderately to $\simeq0.014$ from its initial peak value 0.02. Figure 2(b) shows

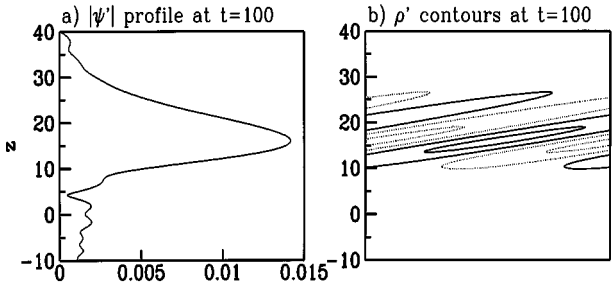

FIG. 2. Simulation at time $t=100$ for case with $N^2=1$ throughout the domain and an initial small-amplitude IGW wavepacket characterized by parameters $A=0.01$, $D=5$; (a) shows the streamfunction amplitude and (b) shows the fluctuation density field by contours of interval 0.01.

contours of the fluctuation density field by intervals of 0.01 with positive (negative) contours illustrated by solid (dashed) lines. The diagram demonstrates that the wavepacket remains well defined and compact but has translated upward from being centered about $z=-20$ to having a peak value at $z\simeq16.0$. For the numerically simulated IGW wavepacket at $t=100$, the characteristics of which are given in the first row of Table I, the vertical group velocity $c_{gz+}\simeq0.38$, the frequency $\omega_+\simeq0.81$, and the vertical wavenumber $k_{z+}\simeq-0.72$. These values do not differ greatly from the characteristics of the initial wavepacket, and in this sense, the wavepacket is said to be weakly dispersive.

If $N^2=J$ is sufficiently small above $z=0$, negligible energy is transmitted into this region by IGW. If $\sqrt{J}$ is moderately smaller than the frequency of the incident wavepacket, however, some proportion of it may be transmitted due to transient forcing. Nonlinear simulations of small-amplitude wavepackets support this assertion. In particular, a simulation is performed for an initial IGW wavepacket characterized by $A=0.01$ and $D=5$, and the background stratification is given by equation (1) with $R=0$ and $J=0.6$ so that N decreases discontinuously at $z=0$ to a frequency smaller than that of the incident wavepacket. Nonetheless, a small-amplitude IGW wavepacket propagates upward above $z=0$ at late times in the simulation. This is demonstrated in Figure 3 which shows contours of the fluctuation density field at times (a) $t=0$, (b) 50, and (c) 100. At each time contours are given by intervals of 0.01. Figure 3(b) shows that the incident wavepacket with upward left to right phase tilt is inhibited from propagating above the evanescent level. The reflected wavepacket at $t=100$ has a downward left to right phase tilt and amplitude almost as large as that of the initial wavepacket. At this time, however, a small-amplitude upward propagating wavepacket with upward left to right phase tilt is also apparent above $z=0$. The direction of propagation of the wavepacket is demonstrated explicitly in Figure 4 which shows horizontally offset profiles of the Reynolds stress τ at 21 successive times $t=0$, 5, 10,…,100. Each vertical profile is illustrated by short dashed lines, except for those at times $t=0$, 50, and 100 which are illustrated by solid lines. The diagram clearly shows the upward flux of horizontal momentum at the beginning of the simulation followed by the reflection and partial transmission of the wavepacket at

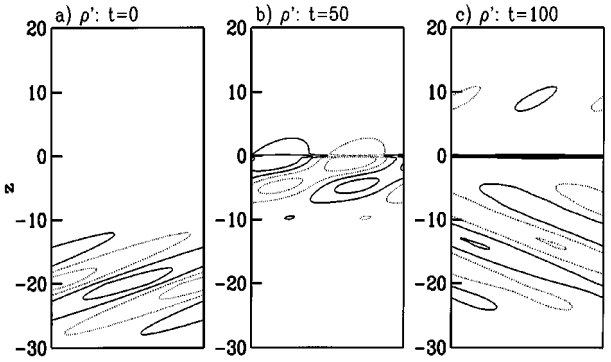

FIG. 3. Fluctuation density field shown in contours by interval of 0.01 for a simulation performed with parameters $A=0.01$, $D=5$, and $J=0.6$ at times (a) $t=0$, (b) 50, and (c) 100. Although the buoyancy frequency above $z=0$ is smaller than the frequency of the initial wavepacket, upward propagating IGW above $z=0$ are apparent at time $t=100$.

late times. The characteristics of the transmitted and reflected wavepackets are given in Table I. These show that the reflected wavepacket moves downward with group velocity comparable in magnitude to the group velocity of the initial wavepacket, but that the transmitted wavepacket moves upward at a slower speed. Because the initial wavepacket propagates with the largest vertical group velocity possible for plane IGW, the transmitted wavepacket is expected to propagate upward more slowly if its wave characteristics are different. Indeed, it is composed of waves that are more vertically oriented ($k_{z+}\simeq -0.38 > -\sqrt{2}/2$) and which propagate with moderately smaller frequency ($\omega_+\simeq 0.72 < \sqrt{2/3}$) than that of the initial wavepacket.

If the initial wavepacket is of large amplitude, the proportion of it that is transported across the evanescent level is significantly larger. This is demonstrated qualitatively in Figure 5, which shows contours of the fluctuation density field by intervals of 0.15 at times $t=0$, 50, and 100 in diagrams

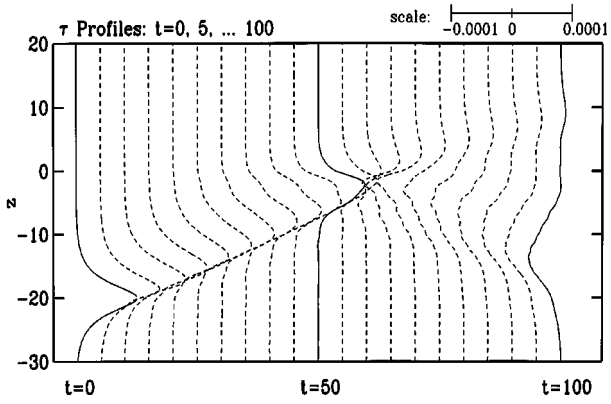

FIG. 4. A sequence of Reynolds stress profiles for a simulation with $A=0.01$, $D=5$, and $J=0.6$. 21 profiles are shown from left to right at times $t=0$, 5, 10, ... , 100. Profiles are shown by solid curves at times $t=0$, 50, and 100, and by dashed curves otherwise. The scale at the top right-hand corner indicates the range of the Reynolds stress for each profile. The diagram illustrates the upward propagation of the initial wavepacket with positive Reynolds stress and the upward (downward) propagation of the transmitted (reflected) wavepackets with positive (negative) Reynolds stress at late times.

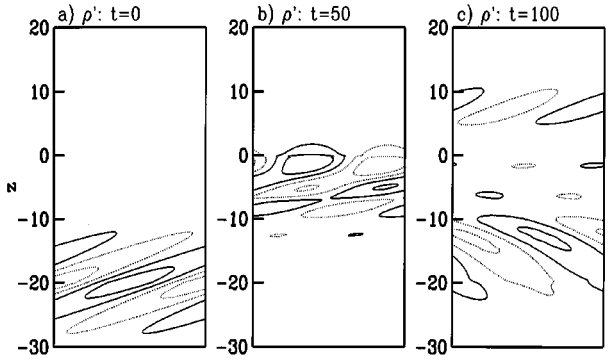

FIG. 5. Fluctuation density field shown as in Figure 3, but for a simulation with $A=0.15$, $D=5$, and $J=0.6$ at times (a) $t=0$, (b) 50, and (c) 100. Contours are shown by an interval of 0.15

(a), (b), and (c), respectively. At $t=50$, Figure 5(b) clearly shows the behavior of the wavepacket as it is inhibited from propagating into the region above $z=0$, where it is evanescent. Nonetheless, at $t=100$, Figure 5(c) shows both a reflected downward propagating and a transmitted upward propagating wavepacket. The direction of propagation may be inferred from the contour plots by the phase tilt of the waves but is demonstrated explicitly in Figure 6, which shows horizontally offset profiles of the Reynolds stress at 21 successive times $t=0$, 5, 10, ... , 100. Each vertical profile is illustrated by short dashed lines, except for those at times $t=0$, 50, and 100 which are illustrated by solid lines. The figure shows two peaks in the Reynolds stress profiles after time $t\simeq 75$ s one positive above $z=0$ moving upward and one negative below $z=0$ moving downward. Unlike the small-amplitude case (Figure 4), here the positive Reynolds stress associated with the transmitted wavepacket is much larger in comparison with the magnitude of the negative Reynolds stress associated with the reflected wavepacket. The characteristics of the waves at the end of the simulation are listed in Table I. For the transmitted wavepacket, the vertical group velocity $c_{gz+}\simeq 0.26$; for the reflected wavepacket, $c_{gz-}\simeq 0.28$. Both values are significantly smaller than the group velocity of the initial wavepacket. The transmitted waves, of vertical wavenumber $k_z\simeq -0.61$, have greater vertical phase tilt, and their frequency $\omega_+\simeq 0.68$ is

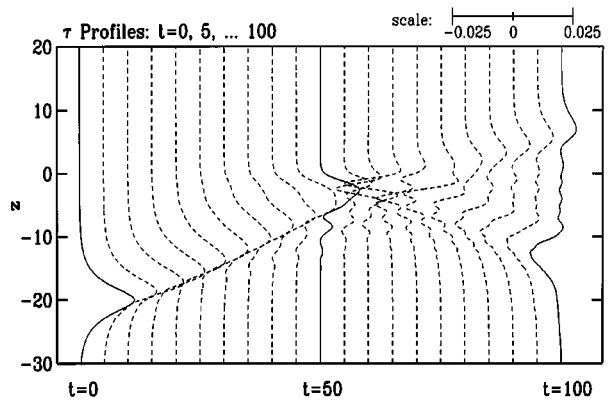

FIG. 6. A sequence of Reynolds stress profiles shown as in Figure 4, but for a simulation with $A=0.15$, $D=5$, and $J=0.6$.

smaller than the frequency of the initial waves and marginally smaller than the buoyancy frequency $\sqrt{J}$ above $z=0$. The characteristics of a wavepacket that evolves from the same initial state but propagates under the effects of dispersion alone in uniformly stratified fluid are listed in Table I for comparison. In the absence of an evanescent level, the wavepacket propagates upward at larger group velocity (although smaller than that expected for a small-amplitude wavepacket), and its frequency is significantly larger. The vertical wavenumber, however, is comparable.

If the initial wavepacket is of small amplitude, linear theory may be employed to estimate the proportion of the wavepacket that is reflected from a weakly stratified region where $N^2=J$. This is done by decomposing the vertical structure of the wavepacket into vertical Fourier components, determining its power spectrum, and integrating over those components with frequency greater than $\sqrt{J}$ to get the proportion of the wavepacket that is reflected. Explicitly, the vertical Fourier transform of the initial wavepacket given by equation (2) is

$$\hat{\psi}(m)=\int dz\,\psi(z)\,\exp(-\imath mz)$$

$$=\frac{2AD}{1+[D(m-k_z)]^2}\,\exp(\imath k_x x), \tag{19}$$

from which the power spectrum is defined:

$$\mathscr{P}\propto|\hat{\psi}(m)|^2. \tag{20}$$

This is normalized so that $\int_{-\infty}^{\infty}\mathscr{P}dm=1$. Thus, the proportion of the wavepacket with vertical wavenumbers exceeding some critical value m_c is

$$\mathscr{R}=\int_{m_c}^{\infty}\mathscr{P}dm=\frac{1}{2}-\frac{1}{\pi}\frac{D(m_c-k_z)}{1+[D(m_c-k_z)]^2}$$

$$-\frac{1}{\pi}\tan^{-1}[D(m_c-k_z)]. \tag{21}$$

If the wavepacket is incident from below on a weakly stratified region where $N^2=J$ and supposing that those Fourier components corresponding to IGW of frequency $\omega<\sqrt{J}$ are entirely transmitted into this region and that the remaining components are entirely reflected, then setting

$$m_c=-k_x\sqrt{\frac{J_B}{J}-1}, \tag{22}$$

equation (21) represents the proportion of the initial wavepacket that is reflected.

In the limit $D\to\infty$ of a wavepacket of infinite vertical extent (plane waves), $\mathscr{R}\to 1$ if $m_c<k_z$ and $\mathscr{R}\to 0$ if $m_c>k_z$; plane waves are either entirely transmitted or reflected depending on whether the buoyancy frequency in the far field is, respectively, greater than or less than the frequency of the initial wavepacket. A compact wavepacket (D finite) is capable of partial transmission, however, due to the transient nature of the disturbance.

The reflection coefficient could more physically have been defined in terms of the energy spectrum $\mathscr{E}\propto(k_x^2+m^2)|\hat{\psi}(m)|^2$, or in terms of the spectrum $\mathscr{M}$ associated with the horizontal wave pseudomomentum for which, using equation (17) for small-amplitude waves, it can be shown that $\mathscr{M}\propto(k_x^2+m^2)^{(3/2)}|\hat{\psi}(m)|^2$. If $Dk_z\gg 1$, however, $|\hat{\psi}(m)|^2$ is sharply peaked about $m=k_z$, and the normalized integrals of these two spectra are both approximately equal to that for the power spectrum.

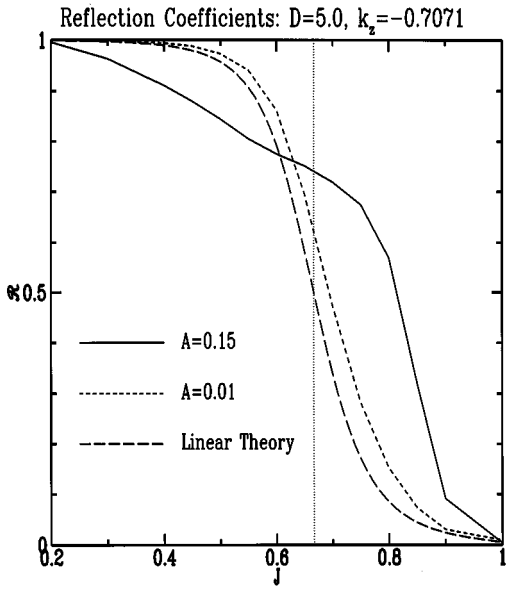

FIG. 7. Reflection coefficients calculated as a function of J for simulations with $D=5$ and $A=0.15$ (solid curve), $A=0.01$ (short dashed curve). The reflection coefficients predicted from linear theory are represented by the long dashed curve. The vertical dotted line indicates the critical value of $J=J_c=\frac{2}{3}$, below which the plane IGW are evanescent above $z=0$. This diagram demonstrates that the transmission of IGW by finite-amplitude wavepackets is dominantly a nonlinear effect.

Figure 7 shows the reflection coefficient $\mathscr{R}$ as a function of the squared buoyancy frequency J above $z=0$ calculated from nonlinear simulations of a large-amplitude wavepacket with $A=0.15$ and $D=5$ (solid line), and a small-amplitude wavepacket with $A=0.01$ and $D=5$ (short dashed line), and these are compared against the linear theory prediction given by equations (21) and (22) (long dashed line). The dotted vertical line indicates the critical value of $J=J_c\simeq\frac{2}{3}$ which equals the squared frequency of the initial wavepacket. For J below this value, the wavepacket is incident upon an evanescent level. For all J, the reflection coefficients determined from the simulation initialized with a small-amplitude wavepacket are comparable to those predicted by linear theory. The latter slightly underpredicts the amount of reflection because it does not account for the behavior of waves near a caustic. The theoretically predicted curve and the curve determined for a small-amplitude wavepacket deviate significantly, however, from that determined from the simulation initialized with a large-amplitude wavepacket. When $J\lesssim J_c$ less reflection occurs and when $J\gtrsim J_c$ more reflection occurs. This figure demonstrates that nonlinear effects may significantly enhance the transmission of energy across the evanescent level.

In order to develop a better understanding of how the transmission mechanism operates, a simulation is performed, initialized with a wavepacket of larger vertical extent. Figure

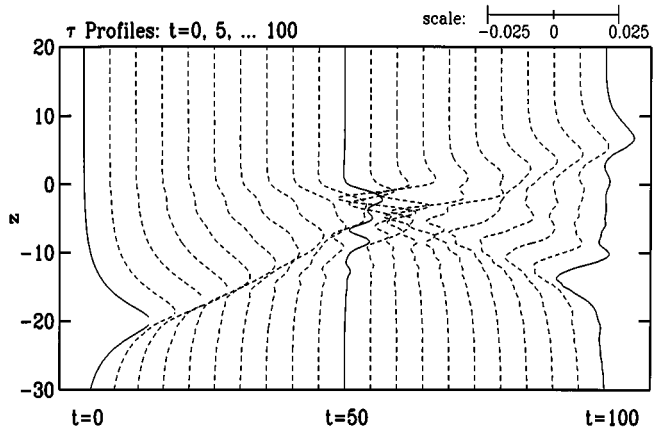

FIG. 8. A sequence of Reynolds stress profiles shown as in Figure 4, but for a simulation with $A=0.15$, $D=8$, and $J=0.6$.

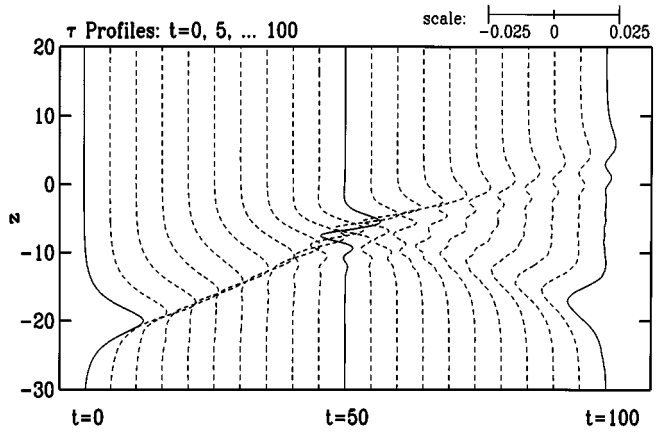

FIG. 10. A sequence of Reynolds stress profiles shown as in Figure 4, but for a simulation with $A=0.15$, $D=5$, and continuously varying N^2 with $R=10$ and $J=0.6$.

8 shows horizontally offset profiles of the Reynolds stress at 21 successive times $t=0$, 5, ...,100, for a simulation with the initial wavepacket characterized by $A=0.15$ and $D=8$. The solid curves represent the profiles at $t=0$, 50, and 100, which otherwise are represented by dashed curves. In comparison with the simulation for $D=5$ (i.e., Figure 6), the reflected and transmitted wavepackets are more sharply peaked, although their characteristics listed in Table I are comparable. Figure 9 compares the reflection coefficients calculated in the case for $D=5$ (solid line) with those for $D=8$ (dashed line). The coefficients are negligibly different except when $\sqrt{J}$ is close to the frequency of the initial wavepacket in which case $\mathscr{R}$ is smaller, indicating that a wavepacket of larger vertical extent reflects less from $z=0$.

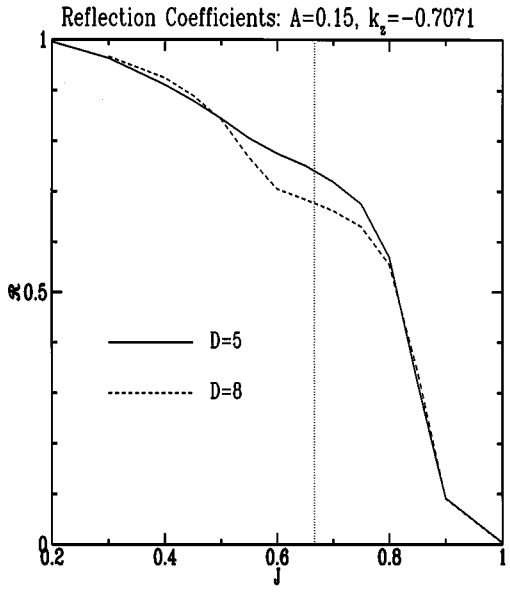

FIG. 9. Reflection coefficients calculated as a function of J shown as in Figure 7, but for simulations with $A=0.15$ and $D=5$ (solid curve), $D=8$ (dashed curve).

Every simulation considered above supposes that N^2 decreases discontinuously to J at $z=0$. The transmission of waves is not sensitive to this feature, however, as shown qualitatively in Figure 10 in which horizontally offset profiles of the Reynolds stress are plotted for 21 successive times $t=0$, 5, ..., 100, in a simulation with $A=0.15$ and $D=5$, and N^2 given by equation (1) with $R=10$ and $J=0.6$. The solid curves represent profiles for $t=0$, 50, and 100, which otherwise are represented by dashed curves. Compared with Figure 6, the profiles demonstrate that the reflected and transmitted waves undergo more dispersion than do IGW for the case in which N^2 changes discontinuously, although the momentum flux associated with the transmitted wavepacket is comparable in both cases. Table I shows that the group velocity and frequency of the transmitted wavepacket are only moderately smaller than the corresponding wave characteristics in the discontinuous N^2 case. Figure 11, which compares the reflection coefficients as a function of J for simulations with a discontinuous N^2 profile (solid line) and a continuous N^2 profile with $R=10$ (dashed line), shows that there is little difference between the proportion of the initial wavepacket that is transmitted in these two cases.

An explanation for some of these quantitative results is provided in the next section.

IV. EXAMINATION OF THE IGW TRANSMISSION MECHANISM

In brief, the nonlinear generation mechanism depends crucially on the adjustment of the mean-flow due to the passage of IGW of finite vertical extent. For example, consider an upward propagating IGW wavepacket of frequency ω_0 and horizontal phase speed $c_{px}=\omega_0/k_x$, incident upon an evanescent level at $z=0$. Thus, above $z=0$ the buoyancy frequency $\sqrt{J}<\omega_0$. Initially, the leading edge of the wavepacket is of small amplitude and the mean-flow changes negligibly. As the centre of the wavepacket, which is of large amplitude, approaches $z=0$ the mean-flow is accelerated. During this time the effective horizontal phase speed of the

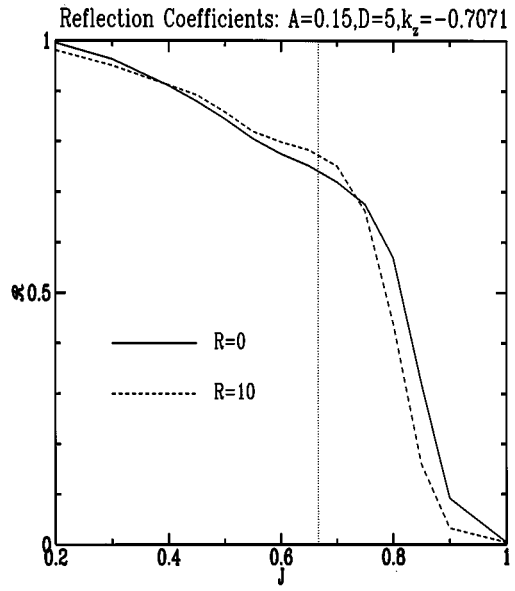

FIG. 11. Reflection coefficients calculated as a function of J shown as in Figure 7, but for simulations with $A=0.15$, $D=5$, and N^2 decreasing from $J_B=1$ to J over distance $R=0$ (solid curve) and $R=10$ (dashed curve).

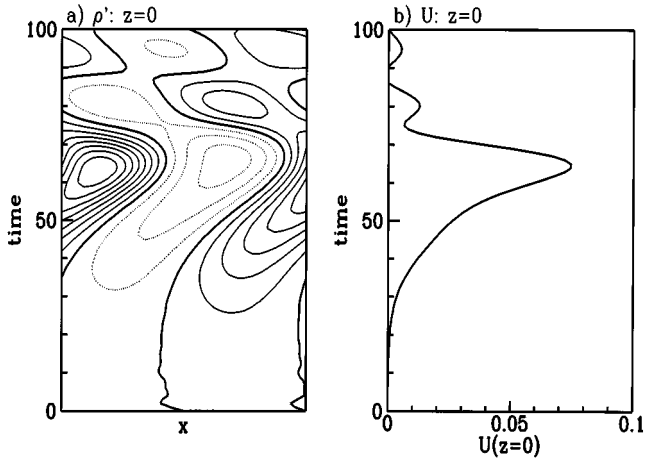

FIG. 12. (a) Hovmoeller diagram of perturbation density field at $z=0$ between times $t=0$ and 100 for a simulation with $A=0.15$, $D=5$, and N^2 discontinuous with $J=0.6$. Contours are shown by intervals of 0.05, the heavy solid line representing the zero contour. (b) Wave induced mean-flow at $z=0$ over the same times.

waves near $z=0$ is larger than c_{px}. Thus, as the mean-flow accelerates the waves constitute a horizontally periodic disturbance at the evanescent level of frequency $\omega>\omega_0>\sqrt{J}$, and the generation of propagating IGW above $z=0$ is further inhibited. However, as the centre of the wavepacket reflects downward and the trailing edge of the wavepacket is incident at $z=0$, the amplitude of the wavepacket decreases and the mean-flow decelerates. During this time the effective horizontal phase speed of the waves is smaller than c_{px} and the waves constitute a horizontally periodic disturbance of frequency $\omega<\omega_0$. If $\omega\leqslant\sqrt{J}$, the disturbance is capable of efficiently generating propagating IGW above $z=0$.

This process is illustrated explicitly by a closer examination of a simulation performed with an initial wavepacket characterized by $A=0.15$ and $D=5$, and with N^2 changing discontinuously from 1 to $J=0.6$ at $z=0$. The results of this simulation have already been illustrated briefly by Figures 5 and 6. Figure 12 demonstrates the relationship between the phase of the waves and the wave induced mean-flow. In (a) contours of the fluctuation density at $z=0$ are shown between times $t=0$ and 100 by way of a Hovmoeller diagram. Contours are given by intervals of 0.05, and these are shown with respect to a reference frame moving at approximately the same speed as the horizontal phase speed of the initial wavepacket, $c_{px}\simeq 0.8165$. In general, the positive fluctuation density is larger than the magnitude of the negative fluctuation density because the former is a measure of upward displacement of parcels from strongly stratified fluid below $z=0$ and the latter is a measure of the downward displacement of parcels from weakly stratified fluid. Similar diagrams indicating the evolution in time of the fluctuation density moderately below or above $z=0$ exhibits the expected symmetry between positive and negative contours. The Hovmoeller diagram of ρ' at $z=0$ shows that at early times IGW appear to grow in amplitude without moving horizontally in the moving reference frame. The phase of the waves shifts forward substantially between $t=35$ and 65, during which time the penetration of waves above the evanescent level is further inhibited. The change in frequency of the waves $\Delta\omega$ at $z=0$ due to the effective increase in the phase speed can be estimated from the slope of the zero contour: $\Delta\omega\lesssim 0.1$. For $t\gtrsim 65$, while the trailing edge of the wavepacket is incident upon the evanescent level, the phase of the waves near $z=0$ shifts backward and a propagating wavepacket is generated above $z=0$. The change in frequency over this time is estimated to be $\Delta\omega\lesssim -0.5$.

The change in phase of the waves at $z=0$ between times $t=0$ and 100 is compared with the wave induced mean-flow shown in Figure 12(b). The figure explicitly shows the acceleration of the mean-flow as the wavepacket grows in amplitude and shifts forward in phase, and it shows how the mean-flow decelerates as the amplitude of the reflected wavepacket decreases and the waves shift backward in phase. The nonlinear generation of IGW above an evanescent level occurs, therefore, when the frequency of the IGW is effectively reduced by the deceleration of the wave induced mean-flow. As expected near a caustic moderately below $z=0$, the wave amplitude is larger and, therefore, the frequency shift due to this nonlinear effect is more pronounced.

Qualitatively this answers the question as to how IGW are transmitted by nonlinear effects. These observations may be put on more quantitative ground, however, by providing a link between the speed of the mean-flow and the amplitude of the waves. For inviscid, Boussinesq flow it is well known that the acceleration of the mean-flow may be expressed in terms of fluctuations of the horizontal velocity u' and vertical velocity w' (for example, see Craik,[24] Sec. 11.5). In nondimensional units,

$$\frac{\partial}{\partial t}\bar{U}=-\frac{\partial}{\partial z}\overline{u'w'}. \tag{23}$$

The right-hand side of the equation is just the negative di-

vergence of the Reynolds stress τ. Thus the mean-flow is accelerated in proportion to the square of the IGW amplitude. To determine the speed of the mean-flow at a particular time from equation (23), however, the Reynolds stress divergence at a particular level must be integrated in time.

The mean-flow speed in time is estimated for a weakly dispersive IGW wavepacket in the following way. Suppose a wavepacket is initially given by

$$\psi_0(x,z) = 2\ \mathrm{Re}\ \{\Phi(z)\ \exp\ [\imath(k_x x + k_z z)]\}, \tag{24}$$

and assume that the vertical structure of the amplitude changes negligibly in time as the wavepacket moves upward at group velocity c_{gz} so that $\psi(x,z,t) \simeq \psi_0(x, z - c_{gz}t)$. Then, in the absence of any initial background motion, equation (23) gives

$$\bar{U}(z,t) \simeq \int_0^t d\tilde{t}\, 4k_x k_z \Phi(z - c_{gz}\tilde{t})\Phi'(z - c_{gz}\tilde{t})$$

$$= \frac{2}{c_{gz}}\ k_x k_z [\Phi^2(z) - \Phi^2(z - c_{gz}t)]. \tag{25}$$

In particular, this demonstrates that no acceleration of the background flow occurs if the initial IGW amplitude $\Phi(z)$ is constant: monochromatic plane waves do not change $\bar{U}$. Conversely, a compact wavepacket may accelerate the background flow to speeds as great as $\bar{U}_{\max} \simeq 2k_x k_z \Phi^2{}_{\max}/c_{gz}$. A numerical check on these predictions is given by a simulation with the initial wavepacket characterized by parameters $A = 0.15$ and $D = 5$. In uniformly stratified fluid with $N^2 = 1$ (not shown here), the observed peak of the mean-flow near $z = 0$ is close to the predicted value $\bar{U}_{\max} \simeq 0.037$. In non-uniformly stratified fluid with $N^2 = J$ above an evanescent level at $z = 0$, the maximum amplitude of the incident and reflected IGW together near $z = 0$ is approximately twice the maximum amplitude of the initial wavepacket. Therefore, $\bar{U}_{\max}$ is approximately four times larger. This explains why the background flow shown in Figure 12(b) is accelerated to such a large extent between times 35 and 65.

An explicit connection between the wave amplitude and the wave induced mean-flow, which is valid in general, may be attained by considering the horizontal pseudomomentum of the waves. If N^2 is constant, equation (17) for the horizontal wave pseudomomentum simplifies to

$$M = -\rho' \omega'. \tag{26}$$

For small-amplitude waves this quantity is horizontally uniform and, as pointed out by Scinocca and Shepherd,[23] equation (18) simplifies to

$$\bar{\mathscr{F}}_z \simeq \tau. \tag{27}$$

Even for large-amplitude IGW in non-uniformly stratified fluid, $\bar{\mathscr{F}}_z = \tau + O(a^3)$ for waves of amplitude a. For $a \lesssim 0.3$, therefore, the vertical flux of horizontal pseudomomentum is negligibly different from the Reynolds stress. It follows from equations (23) and (16) that the horizontal pseudomomentum is negligibly different from the horizontal mean-flow to within a constant determined by the initial conditions. That is

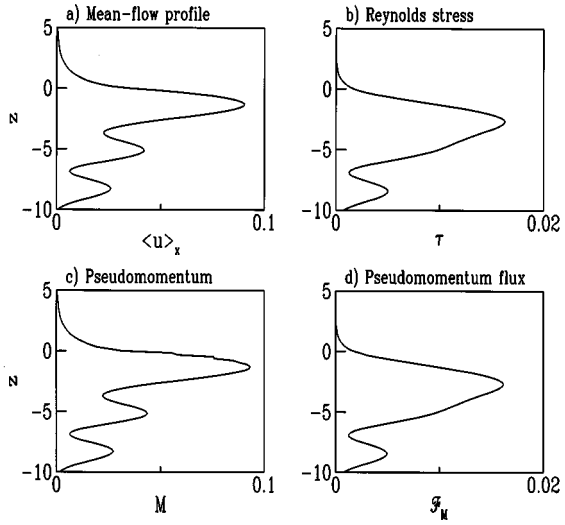

FIG. 13. A comparison at time $t = 50$ for $-10 \leqslant z \leqslant 5$ of (a) the horizontally averaged mean-flow with (c) the horizontal pseudomomentum of waves, and of (b) the Reynolds stress with (d) the vertical flux of horizontal pseudomomentum. The profiles are taken from a simulation with $A = 0.15$, $D = 5$, and N^2 discontinuous with $J = 0.6$.

$$\bar{U}(z,t) - \bar{U}_0 = M - M_0 \simeq -[\rho' \omega'|_t - \rho' \omega'|_{t=0}]. \tag{28}$$

It is well established that the Lagrangian counterpart of this result is exact,[19] specifically that the generalized Lagrangian mean of the velocity is precisely equal to the pseudomomentum in non-rotating, non-dissipative, and adiabatic flows. However, the conditions under which this result in a Lagrangian framework may be extended to an Eulerian framework are less clear, and it is fortuitous that such a straightforward connection between the wave induced mean-flow and the horizontal pseudomomentum in Eulerian variables can be derived for the case of Boussinesq (and anelastic) IGW.

It is interesting to examine the limit of equation (28) for small-amplitude waves of the form of equation (24). Defining ρ' and ω' in terms of the streamfunction using equations (3) and (12), respectively, gives

$$-\rho' \omega' \simeq 2\frac{|\vec{k}|^2}{c_{px}} |\Phi(z)|^2. \tag{29}$$

Substituting the plane IGW expressions for c_{px} and c_{gz}, this reduces to the approximation derived from time integrating the Reynolds stress as expressed in equation (25).

Figure 13 shows the profiles of (a) the mean-flow and (b) the Reynolds stress at time $t = 50$ for a simulation with an initial wavepacket characterized by parameters $A = 0.15$ and $D = 5$, and with discontinuous N^2 such that $J = 0.6$ above $z = 0$. These profiles are compared with those of (c) the horizontal pseudomomentum and (d) its vertical flux calculated at the same time using equations (17) and (18), respectively. There is no distinguishable difference between the Reynolds stress and pseudomomentum flux profile, and the horizontal pseudomomentum itself differs from the horizontal mean-flow only near $z = 0$ where N^2 is discontinuous. The rapid variations of the pseudomomentum profile are attributed to

the round-off error that is significant near $z=0$ where the difference between large numbers is calculated.

V. DISCUSSION AND CONCLUSIONS

The qualitative understanding of the nonlinear generation mechanism helps to explain many of the results regarding the reflection coefficients calculated as a function of the squared buoyancy frequency J above $z=0$. If the frequency of the initial wavepacket $\omega \gtrsim \sqrt{J}$, then $z=0$ is an evanescent level and wave reflection is anticipated. Transmission of large-amplitude waves is enhanced, however, by the reduction of the wave frequency that occurs when the wave induced mean-flow decelerates as the incident wavepacket reflects. Conversely, if the frequency of the initial wavepacket $\omega \lesssim \sqrt{J}$, then wave transmission is anticipated. More reflection of large-amplitude waves occurs, however, because the wave frequency increases when the wave induced mean-flow accelerates as the wavepacket is incident upon the level $z=0$. Because a wavepacket reflects from an evanescent level over a longer time if its vertical extent is larger, the forcing frequency at this level is smaller, and the transmission mechanism is further enhanced.

In light of the relationship drawn between the phase of the waves and speed of the mean-flow, as illustrated by Figure 12, a crude estimate may be established of the degree to which nonlinearity enhances the transmission mechanism. Assuming the adjustment to the phase speed Δc_p is directly proportional to the acceleration of the wave induced mean-flow, then

$$\Delta c_p = \mathscr{T} \frac{\partial M}{\partial t}, \tag{30}$$

in which M is the horizontal wave pseudomomentum given by equation (17) and $\mathscr{T}$ is the characteristic time-scale of variations in M. That is

$$\mathscr{T} \simeq O\left(\left[\frac{1}{M} \frac{\partial M}{\partial t} \right]^{-1} \right). \tag{31}$$

Combined with equation (30), the increase in frequency due to nonlinear effects as the leading edge of the wavepacket is incident at $z=0$ is estimated in terms of the structure of the initial wavepacket with horizontal pseudomomentum $M_0(z)$ by

$$\Delta \omega \simeq k_x [M_0(z_0) - M_0(z \to \infty)] \simeq 8 \frac{|\vec{k}|^2}{c_{px}} A^2. \tag{32}$$

Similarly, by the symmetry of the incident wavepacket considered here, the decrease in frequency due to nonlinear effects as the trailing edge of the wavepacket is incident at $z=0$ is approximately $\Delta \omega$. This estimate underpredicts the actual change in frequency because it does not take into account the increase in amplitude of the disturbance near a caustic. Nonetheless, for the parameters $A=0.15$, $\vec{k}=(1,-\sqrt{2}/2)$, and $c_{px}=\sqrt{2/3}$, equation (32) gives $\Delta \omega \simeq 0.3$, which is of the same order as that estimated from the Hovmoeller diagram for this case (Figure 12). Therefore, significant nonlinear enhancement of wave transmission across an evanescent level or of wave reflection from a level where $\omega \gtrsim \sqrt{J}$ should occur when $|J - J_c| \lesssim \Delta \omega$. This predicted range of enhancement agrees well with the range over which the reflection coefficient calculated for simulations with a large-amplitude wavepacket (i.e., Figure 7) deviates significantly from linear theory. A better estimate of the range of enhancement could, perhaps, be made by developing an appropriate weakly nonlinear theory for IGW wavepackets of small vertical extent compared with the depth of the strongly stratified region.

Throughout it has been assumed that the initial background flow is constant at all heights. For small-amplitude waves, ray theory predicts that the effect of introducing moderate shear would be to alter the angle of incidence of the wavepacket on the evanescent level, the angle being more horizontal as the wavepacket approaches a level of the background flow with speed closer to that of the phase speed of the waves. This behavior may have a significant effect upon the fraction of energy that is transmitted across an evanescent level. With or without the presence of background shear, however, the transmission of a compact IGW wavepacket across an evanescent level is amenable to experimental study, and this is currently under investigation.

These results may have important implications for many geophysical circumstances. Although ducted IGW are often assumed to be trapped within regions of strong stratification, it has been demonstrated that bursts of energy in the form of compact IGW wavepackets may transmit energy away from the duct due to their transient nature and nonlinear effects. Such behavior may already have been observed in numerical simulations such as those performed by Yang and Houze,[25] who, in their study of IGW associated with mid-latitude squall lines, accounted for many of the characteristics of the ducted IGW they observed by linear theory. They remarked, nonetheless, that large-amplitude IGW leaked into the stratosphere but they did not explain the mechanism for this process.

Because it is transient and occurs on short time- and length-scales, observation of the transmission of waves across an evanescent level in the atmosphere or ocean may be challenging. Nonetheless, it is interesting to speculate upon its implications to a particular oceanographic example. IGW have recently been proposed as a possible source of momentum for the deep equatorial countercurrents.[26,27] But if IGW originate near the ocean surface where the energy density is large, it remains unclear how these waves can propagate to great depths below the thermocline where the stratification is weak. The results presented here may help, in part, to resolve this dilemma.

ACKNOWLEDGMENTS

The author would like to thank T. G. Shepherd for his useful comments on the manuscript. This work has been supported in part by the Natural Environment Research Council (NERC), Grant No. GR3/09399.

[1] T. Hauf, "Aircraft observation of convection waves over southern Germany—A case study," Mon. Weather Rev. **121**, 3282, (1993).
[2] J. M. Huthnance, "Internal tides and waves near the continental shelf edge," Geophys. Astrophys. Fluid Dyn. **48**, 81 (1989).

[3]A. E. Gill, ''Models of equatorial currents,'' in *Numerical Models of Ocean Circulation* (National Academy of Science, Washington, DC, 1995), pp. 181–203.
[4]T. B. Benjamin, ''Internal waves of permanent form in fluids of great depth,'' J. Fluid Mech. **29**, 559 (1967).
[5]D. J. Benney, ''Long nonlinear waves in fluid flows,'' J. Math. Phys. **45**, 52 (1966).
[6]H. Ono, ''Algebraic solitary waves in stratified fluids,'' J. Phys. Soc. Jpn. **39**, 1082 (1975).
[7]R. I. Joseph, ''Solitary waves in a finite depth fluid,'' J. Phys. A Math. Gen. **10**, L225 (1977).
[8]T. Kubota, D. R. S. Ko, and L. Dobbs, ''Propagation of weakly nonlinear internal waves in a stratified fluid of finite depth,'' J. Hydronaut. **12**, 157 (1978).
[9]A. R. Osborne and T. L. Burch, ''Internal solitons in the Andaman Sea,'' Science **208**, 451 (1980).
[10]A. K. Liu, J. R. Holbrook, and J. R. Apel, ''Nonlinear internal wave evolution in the Sulu Sea,'' J. Phys. Oceanogr. **15**, 1613 (1985).
[11]R. R. Long, ''Some aspects of the flow of stratified fluids. A theoretical investigation,'' Tellus **5**, 42 (1953).
[12]J. F. Scinocca and W. R. Peltier, ''The instability of Long's stationary solution and the evolution toward severe downslope windstorm flow. Part I: Nested grid numerical simulations,'' J. Atmos. Sci. **50**, 2245 (1993).
[13]F. P. Bretherton, ''Gravity waves in shear,'' Q. J. R. Meteorol. Soc. **92**, 466 (1966).
[14]M. J. Lighthill, *Waves in Fluids* (Cambridge University Press, Cambridge, England, 1978).
[15]S. F. Dotsenko, ''Anomalous frequency dispersion of internal waves in the ocean,'' Izv. Acad. Sci. USSR Atmos. Ocean. Phys. **29**, 683 (1994).
[16]W. D. Smyth and W. R. Peltier, ''The transition between Kelvin–Helmholtz and Holmboe instability: An investigation of the overreflection hypothesis,'' J. Atmos. Sci. **46**, 3698 (1989).
[17]F. P. Bretherton and C. J. R. Garrett, ''Wavetrains in inhomogeneous moving media,'' Proc. R. Soc. London Ser. A **302**, 529 (1969).
[18]G. B. Whitham, ''A general approach to linear and nonlinear dispersive waves using a Lagrangian,'' J. Fluid. Mech. **22**, 273 (1965).
[19]D. G. Andrews and M. E. McIntyre, ''An exact theory of nonlinear waves on a Lagrangian-mean flow,'' J. Fluid Mech. **89**, 609 (1978).
[20]D. G. Andrews and M. E. McIntyre, ''On wave action and its relatives,'' J. Fluid Mech. **89**, 647 (1978).
[21]M. E. McIntyre and T. G. Shepherd, ''An exact local conservation theorem for finite amplitude disturbances to non-parallel shear flows with remarks on Hamiltonian structure and on Arnol'd's stability theorems,'' J. Fluid Mech. **181**, 527 (1987).
[22]T. G. Shepherd, ''Symmetries, conservation laws, and Hamiltonian structure in geophysical fluid dynamics, ''Adv. Geophys. **32**, 287 (1990).
[23]J. F. Scinocca and T. G. Shepherd, ''Nonlinear wave-activity conservation laws and Hamiltonian structure for the two-dimensional anelastic equations,'' J. Atmos. Sci. **49**, 5 (1992).
[24]A. D. D. Craik, *Wave Interactions and Fluid Flows* (Cambridge University Press, Cambridge, England, 1985).
[25]M-J. Yang and R. A. Houze, Jr., ''Multicell squall-line structure as a manifestation of vertically trapped gravity waves,'' Mon. Weather Rev. **123**, 641 (1995).
[26]J. Muench, E. Kunze, and E. Firing, ''The potential vorticity structure of equatorial deep jets,'' J. Phys. Oceanogr. **24**, 418 (1994).
[27]B. R. Sutherland, ''On the dynamic excitation of internal gravity waves in the equatorial oceans,'' submitted to J. Phys. Oceanogr.